Journal of Colloid and Interface Science 455 (2015) 154–162

Contents lists available at ScienceDirect

Journal of Colloid and Interface Science

www.elsevier.com/locate/jcis

Synthesis of water-soluble gold clusters in nanosomes displaying robust photoluminescence with very large Stokes shift

B. Santiago-González [a], C. Vázquez-Vázquez [a], M.C. Blanco-Varela [a], J.M. Gaspar Martinho [b], J.M. Ramallo-López [c], F.G. Requejo [c], M.A. López-Quintela [a,*]

[a] Laboratorio de Magnetismo y Nanotecnología, Instituto de Investigaciones Tecnológicas, Universidad de Santiago de Compostela, E-15782 Santiago de Compostela, Spain
[b] Centro de Química-Física Molecular and IN – Institute of Nanoscience and Nanotechnology, Instituto Superior Técnico, Universidade de Lisboa, 1049-001 Lisboa, Portugal
[c] Instituto de Investigaciones Fisicoquímicas Teóricas y Aplicadas – INIFTA (CONICET, UNLP), Diagonal 113 y calle 64, 1900 La Plata, Argentina

GRAPHICAL ABSTRACT

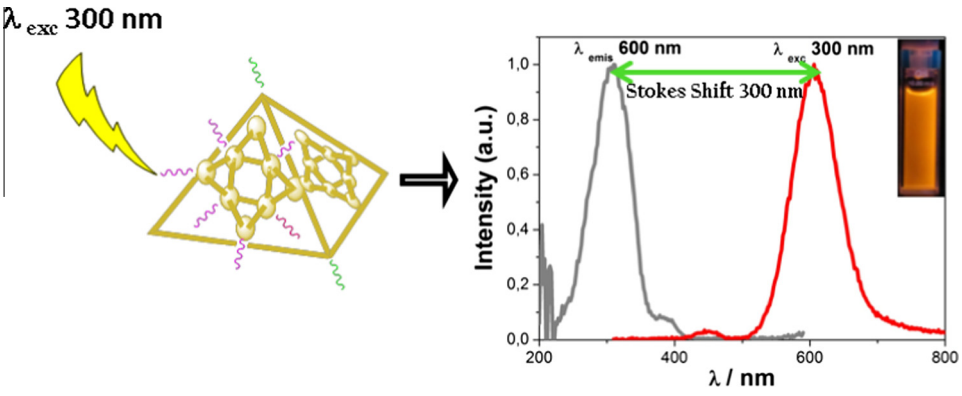

ARTICLE INFO

Article history:
Received 20 April 2015
Accepted 19 May 2015
Available online 29 May 2015

Keywords:
Luminescent gold clusters
Cluster–cluster complexes
Large Stokes shifts
Nanosomes

ABSTRACT

This paper reports a novel procedure using nanosomes, made of bola-hydroxyl and mercapto-palmitic acids, for the production of gold clusters with robust luminescent emissions and very large Stokes shifts. It shows that these results cannot be explained by the currently accepted mechanism based on ligand-to-metal charge transfer absorptions involving electron-rich ligands attached to the cluster core. Exhaustive characterization of the cluster samples using Mass Spectrometry, HR-TEM/STEM, XPS, EXAFS, and steady-state and time-resolved luminescence allows to deduce that a mixture of two cluster sizes, having non-closed shell electronic configurations, are firstly generated inside the nanosome compartments due to the difference in bonding strength of the two types of terminal groups in the fatty acids. This initial bimodal cluster size distribution slowly evolves into very stable, closed-shell Au cluster complexes (Au_6–Au_{16} and Au_5–Au_{14}) responsible for the observed luminescent properties. The very small (≈1.2 nm) synthesized cluster complexes are water soluble and suitable to be used for the conjugation of biomolecules (through the terminal COO^- groups) making these systems very attractive as biomarkers and offering, at the same time, a novel general strategy of fabricating stable *atom-level quantum dots* with large Stokes shifts of great importance in many sensor applications.

* Corresponding author.
E-mail address: malopez.quintela@usc.es (M.A. López-Quintela).

http://dx.doi.org/10.1016/j.jcis.2015.05.042
0021-9797/

1. Introduction

Gold clusters are being intensively investigated due to their many attractive features, such as luminescence [1], catalytic activity [2], ferromagnetism [3], paramagnetism [4], optical chirality [5], etc. Their size-dependent effects are observed due to the confinement of the free electrons relative to the Fermi wavelength in the cluster conduction band [6,7]. This new class of materials, with well-defined number of atoms in their core, seems to compete very favorably in terms of size and toxicity with the well-known semiconductor quantum dots, making them good candidates for different applications, especially for biological sensing [8,9].

The electronic structure of gold clusters change dramatically with size and geometry, having characteristic absorption and emission profiles due to intraband and interband transitions, which do not appear in nanoparticles of the same material. This fact provides the possibility of obtaining color and luminescent tunabilities with clusters from UV to IR [10], which can offer great potential applications of clusters in fields like fluorescence sensing and imaging. Indeed, it has already been reported the use of these new materials for in vitro detection of molecules in solution and in vivo imaging of cells and cellular processes [9,11].

There have been several studies in recent years about luminescent clusters displaying large Stokes shift. Shichibu et al. [12] observed that Au_{13} clusters obtained by treating a polydisperse sample with hydrochloric acid show an emission band at 766 nm by excitation at 360 nm. Shibu et al. [13] prepared Au_{15} trapped in cyclodextrins showing the maximum emission centered at 690 nm when excited at 375 nm. Biang et al. [14] synthesized luminescent Au clusters with a bright red emission and large Stokes shift using both histidine and 11-mercaptoundecanoic acid as stabilizers. Gold clusters were also obtained using ribonuclease A as bio-template showing a large Stokes shift (210 nm) and a high luminescence quantum yield (QY) of 12%, being suitable for cancer targeting and imaging [15]. In the described cases the authors did not investigate the reasons for the observed luminescence. Huang et al. [16] were the first to associate the large Stokes shift and long lifetimes (159/834 ns) observed in mannose-protected Au clusters to the presence of gold nanoclusters/polynuclear Au(I)-thiol (core/shell) complexes. Shang et al. [17] gave a similar explanation for dihydrolipoic acid stabilized Au clusters, whose luminescence decrease by adding more reducing agent to the cluster solution. This was further confirmed by the binding energy (BE) of Au $4f_{7/2}$ that falls between the corresponding values of Au(0) and Au(I). It is assumed that charge transfer states provided by electron rich ligands are responsible for the effective enhance luminescence in clusters, as for example it is assumed to occur in large thiolate protected gold clusters (Au > 18) involving –RS–Au–RS–Au–RS staple motifs [18,19]. Therefore, the presence of large Stokes shifts observed in clusters has been interpreted assuming a similar mechanism based on ligand-to-metal charge transfer (LMCT) absorptions involving electron-rich atoms or groups attached to the cluster core [20–22]. But, a definitive evidence for this mechanism is still lacking. At the same time, the resulting outlook conveys the need of developing new and simple synthetic methods for the production of stable photoluminescent clusters with correspondent improvements in terms of photostability, brightness, large Stokes shifts and appropriate size because they could find applications in many different areas, as in biodiagnostics including sensing, imaging, detection, therapy and monitoring structural changes of biomolecules [23,24].

We will show here that nanosomes, made of bola-hydroxyl and mercapto-palmitic acids acting as capping agents, providing both OH and SH terminal groups in the fatty acids, are excellent templates for the synthesis of clusters with very large Stokes shifts similar to those encountered in rare earth materials. Moreover, we will show that these results *cannot be explained by the usual LMCT mechanism*, but they can be understood assuming the initial formation of two cluster sizes ($Au_{5,6}$ and $Au_{14,16}$), having non-closed shell electronic configurations, due to the difference in bonding strength of the two capping agents, which template the formation of the bimodal cluster size distribution inside the nanosome compartments. Such clusters slowly evolve into very stable, closed-shell Au cluster complexes (Au_6–Au_{16} and Au_5–Au_{14}) with robust luminescence. These cluster systems, due to their very small size (≈1.2 nm) and large Stokes shifts, can be very attractive in sensor applications, like e.g. biomarkers for cellular fluorescence imaging.

2. Results

The nanosomes used for the cluster synthesis were firstly studied by TEM. Results show that the outer diameter is ≈25 nm (SI, Fig. S1). Taking into account the size of the bola lipids, one can deduce that the inner size of the nanosomes is ≈10 nm. The procedure for the synthesis of clusters inside the nanosomes is schematically shown in Fig. 1. Preliminary experiments shown that the ratio of the bola lipid mixture, R1 = [SH]/[OH], and the ratio of the thiol to the Au salt, R2 = [SH]/[Au(III)], have a major influence on the optical properties of the synthesized particles. Therefore, we fixed the values of both ratios (R1 = 0.311 and R2 = 2.60) for the experiments here reported.

Fig. 2 shows the time evolution of the absorption spectrum during the synthesis carried out at pH ≈ 12 (given by the TBAOH solution used for the preparation of nanosomes). It can be observed

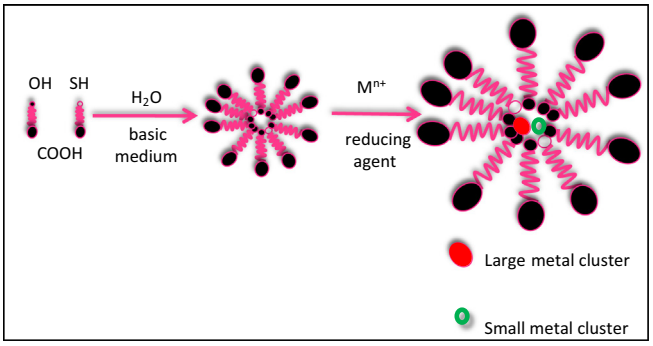

Fig. 1. Schematic representation of the synthetic approach used for the preparation of clusters inside nanosomes.

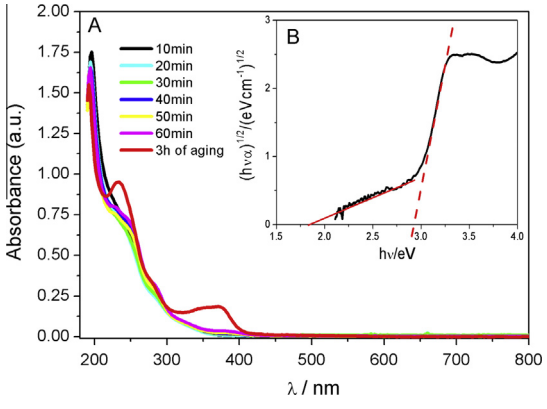

Fig. 2. (A) UV–vis spectra during the synthesis of gold clusters in nanosomes and 3 h later. (B) Tauc's plot derived from the absorption spectrum for the estimation of the cluster band-gap – indirect transition – (Eg = 1.8 eV).

that, after 20 min, new bands start to appear. The final spectrum of the sample after few hours shows absorption bands with the following peak positions: 230, 275, 347 and 372 nm. This clearly indicates the formation of non-metallic clusters and the totally absence of gold nanoparticles in the sample, since no signal of the plasmon band is observed. From the absorption spectrum, assuming a semiconductor-like behavior for the generated gold clusters, one can obtain information of the cluster band-gap by the Tauc's approach [25] used for semiconductors: $(\alpha h\upsilon) = A(h\upsilon - E_g)^n$, where α is the absorption coefficient, h is the Plank constant, υ is the frequency of the radiation, A is a material dependent constant, E_g is the band-gap and $n = 1/2$ (direct transition) or $n = 2$ (indirect transition). In this case, the results fit well with $n = 2$ (indirect transition) and the calculated E_g value is 1.8 eV (Fig. 2). It has to be noticed that the observation of an indirect transition in this nanosome-cluster system is different from previous experiments with clusters, in which the results fitted mostly to a direct transition [26]. From the calculated E_g value one can predict the number of atoms, N, in the clusters using the simple spherical Jellium model: $N = (E_F/E_g)^3 = (5.32\ \text{eV}/1.8\ \text{eV})^3$, where E_F is the Fermi level of gold [27]. From this equation a value of $N \approx 17$ atoms can be obtained.

The size distribution of the synthesized Au clusters has been analyzed by ESI-mass spectrometry because ESI is a much softer technique than LDI and MALDI, so that with the other techniques some fragmentation and aggregations seem to occur [28]. Different ESI techniques (ESI-TOF, ESI-Orbitrap, and micro-ESI-TOF, -see SI-), were used but we will show here only the results obtained using micro-ESI-TOF (see Fig. 3, SI Fig. S2a–g and Table S1) because this is a more sensitive technique (see a more detailed discussion in SI). In any case, all the used techniques seem to agree with the presence of two populations of gold clusters inside the nanosomes. Using the micro-ESI-TOF technique one can clearly distinguish one population of small clusters, mainly with sizes of 5 and 6 atoms and another one with bigger clusters composed of 14–16 atoms (see SI Table S1). It can be observed that this last population approximately matches with the number of atoms previously calculated from the Tauc plot of the last part of the absorption band using the Jellium model (≈17). It is interesting to note that the Tauc plot also shows a linear behavior in the penultimate part of the absorption band (see broken line in the inset of Fig. 2) pointing to the presence of other type of semiconductor clusters in the sample with an E_g value of 2.9 eV. According to the Jellium model this E_g value would also indicate the presence of a population of small Au_N clusters with $N \approx 6$, in a surprising very good agreement with the Mass spectra results.

It is known that exceptional stability of clusters is associated to close-shell electronic structures. This requirement is commonly formulated as $(L_S.Au_NX_M)^z$, $n^* = N\upsilon_A - M - z$, where N is the number of core metal atoms with atomic valency ν_A. The shell-closing electron number (n^*) of the metallic core has to satisfy either one of the shell-closing numbers (2, 8, 18,...) given by the anharmonic spherical mean-field potential quantum model – for 3D clusters – [29] or (2, 6, 8, 12...) given by the planar harmonic quantum dot model with a triangular shape [30] – for planar or quasi-planar clusters –, being z the charge, and the Au core is stabilized by the ligands L and X, where X may withdraw electrons (or localize electrons into covalent bonds) from the metal core, and L can be attached as a weak Lewis base that coordinates to the core surface by dative bonds and does not withdraw electrons from the metal atoms, being needed only for completion of the steric protection of the core surface. Table S1 summarizes the clusters species assigned by the micro-ESI-TOF mass spectra and their corresponding cluster charge, number of electrons per cluster and their electronic structures assuming that clusters below 10–12 atoms preferentially adopt a planar geometry. It can be observed the presence of clusters with both types of close-shell and non-close-shell electronic configurations. We will address and discuss this subject later on.

To further confirm the presence of the two types of clusters in the samples, we carried out EXAFS experiments at the Au L_3 edge.

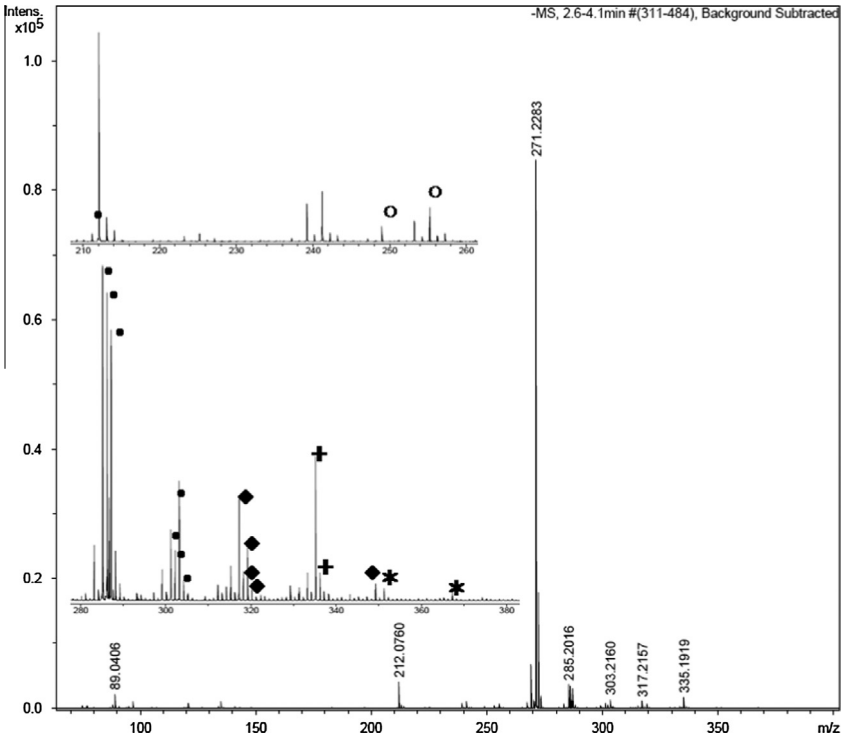

Fig. 3. Micro-ESI-TOF (low mass range) mass spectrum of gold clusters. Inset: amplification showing the identified gold clusters: (•) Au_5, (♦) Au_6, (+) Au_{14}, (○) Au_{15} (∗) Au_{16} – see SI Table S1 for more information about the assigned clusters.

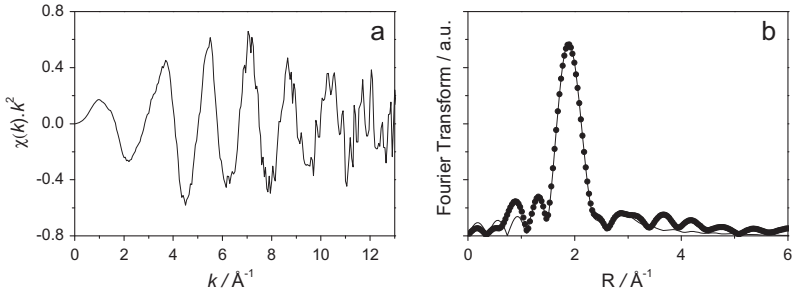

Fig. 4. (a) Au-L3 experimental EXAFS oscillation of gold clusters. (b) Experimental Fourier Transform of the EXAFS oscillation (filled circles) and the corresponding obtained fit for first two coordination shells (solid line).

Four coordination shells have to be proposed to fit the EXAFS data: one for sulfur and one for oxygen, and two for gold atoms around the gold absorber atom. Few constrains were imposed in order to fit the data. In particular, Au–Au coordination numbers were fixed considering Häkkinen predicted structures for gold clusters [29]. Fig. 4 shows the experimental EXAFS oscillation and its corresponding Fourier Transform and fitted function for the first and second coordination shells. The obtained fitting results are shown in Table 1: the first two shells correspond to the two different capping atoms: oxygen and sulfur, located at 1.85 and 2.30 Å from the absorbing gold atom respectively, with an atomic relationship of 1:3. The two fitted Au–Au interatomic distances (2.72 and 3.02 Å – see Table 1 –) nicely correspond to the theoretically predicted values [29] for the two cluster sizes already detected by Mass spectrometry, i.e. one with 5/6 atoms and another composed by 14–16 atoms, which would have a total average coordination number Au–Au between 3.3 and 3.7 as we proposed in our fit. It should be noted the high values of the Debye–Waller factors fitted in these two shells (see Table 1). Those values indicate the dispersion of Au–Au distances, following the same theoretical model predicted for Au clusters [29].

Table 1
Obtained EXAFS fits for Au L3-edge EXAFS experiments. *N*: average coordination number, *R*: interatomic distance, σ2: Debye–Waller factor, E0: threshold energy shifts.

Shell	*N*	*R*/Å	σ2/Å2	E0/eV
O	0.5 (2)	1.85 (4)	0.020(7)	7.4(8)
S	1.8 (1)	2.30 (1)	0.0022(4)	7.4(8)
Au	2.8	2.72 (2)	0.018(2)	7.4(8)
Au	0.7	3.02 (1)	0.008(2)	7.4(8)

TEM images of purified clusters (i.e. free from nanosomes) can be seen in Fig. 5 along with the size histogram and, for comparison, the estimated number of Au atoms for 3D Au_N clusters (a compact spherical model and the bulk density of Au was assumed for such estimations). The average particle diameter (1.2 ± 0.2 nm) should correspond to ≈40 atoms. It is known, however, that the structure of clusters differs from the bulk material, so the number of atoms in the clusters should be much lower. In fact, the observed size is similar to the thiol-functionalized Au_{25} cluster, which is currently one of the most well characterized nanoclusters (see e.g. Varnavski et al. [31], Wu et al. [32]). If we assume this number (25) as the approximate number of atoms in the species observed by TEM, we can see that such estimated size is larger than the detected sizes by mass spectrometry (5/6 and 14/16) – we will come back to this issue later on –. It can be noticed that the size of the purified clusters is one order of magnitude lower than the nanosome compartments, clearly indicating that the nanosome size does not template the cluster size, and that other factors are involved in the cluster formation, as we will discuss later.

Fig. S3 in SI shows the HRTEM image of the sample after some time of irradiation with the strong electron beam. The crystalline structure is now observed showing lattice planes separated by 0.234 nm corresponding to the face-centered cubic Au (1 1 1). In the same picture it can be observed that clusters, which have not been so strong irradiated, do not show such crystallinity indicating that clusters fuse under the electron beam irradiation, as it was

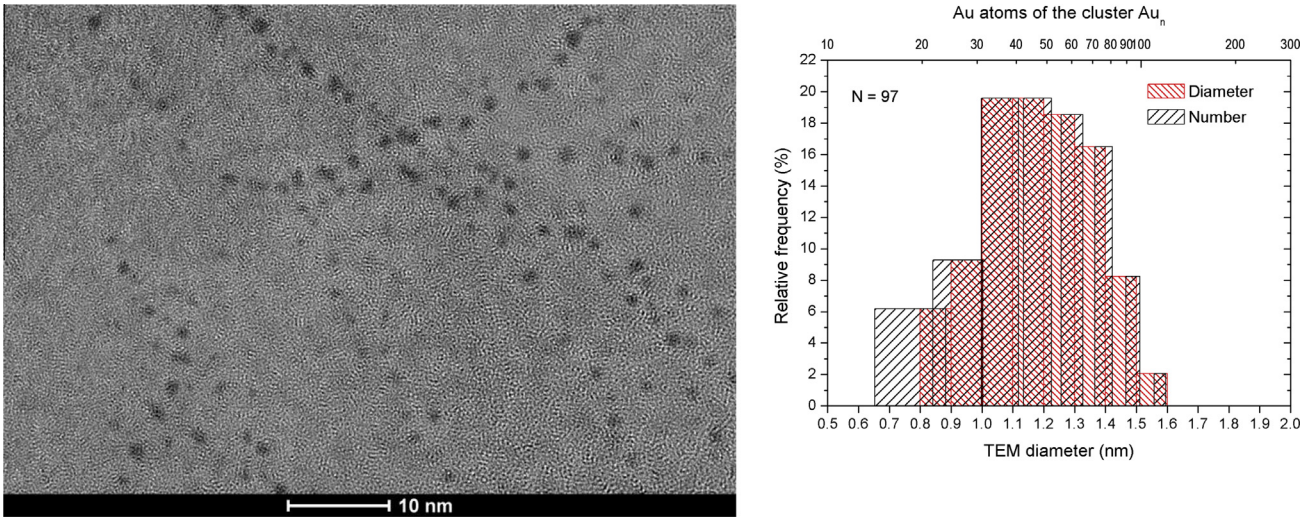

Fig. 5. HR-TEM image of the synthesized gold clusters and the corresponding size histogram (red stripes). The corresponding number of Au atoms assuming a 3D compact structure is also shown (black stripes). (For interpretation of the references to color in this figure legend, the reader is referred to the web version of this article.)

reported before [33]. Therefore, other *softer* microscopy techniques, like STEM (scanning transmission electron microscopy), were used for imaging the clusters without fusing. HAADF (high-angle annular dark field)-STEM images of the samples show individual clusters with atom resolution with similar sizes than the determined by TEM (SI, Fig. S4), but even with this technique splitting of atoms from clusters cannot be avoided.

The oxidation state of the gold clusters was determined by X-ray photoelectron spectroscopy (XPS) (see SI Figs. S5 and S6). Gaussian fitting indicates the presence of only one oxidation state. The binding energy value obtained for Au $4f_{7/2}$ was 84.2 eV, which corresponds to Au(0) – see Table S3 –, and clearly indicates the complete reduction of the gold salt. The binding energy of S $2p_{3/2}$ was also determined, (see SI Fig. S6) showing two contributions: 161.8 eV corresponding to sulfur bounded to Au, and 163.27 eV corresponding to thiol groups unbounded or free. The oxygen detected is also bounded to carbon forming C–O bonds and also C=O–N bonds [34–36], confirming the external presence of TBA (providing the steric protection, and rendering the acids soluble in water). Another proof that Au in the cluster species is mainly in the form of Au(0) is given by the fact that the optical properties of the Au clusters do not change after adding more reducing agent once the Au clusters are formed.

Gold clusters exhibit photoluminescence distributed by a high-energy band centered at 450 nm (2.76 eV) and a low-energy band centered at 600 nm (2.07 eV), as it is shown in Fig. 6 for samples at pH ≈ 12. It is interesting to note that both emission bands are very close to the band-gaps (2.9 eV and 1.8 eV) deduced before for the small and large clusters, respectively, suggesting that these bands could be related to the emission of the small and large clusters, respectively. The relative intensity of the two bands is strongly dependent on the excitation wavelength (and also on the synthesis conditions, as it will be shown later), as it was observed by the differences in the photoluminescence spectra by excitation at 300 and 410 nm. The excitation spectra collected at 450 nm and 600 nm show two bands centered at 410 nm and 300 nm, whose intensities vary with the emission wavelength. A closer analysis of the excitation spectra shows that the high-energy emission band displays the corresponding absorption band with a usual small Stokes shift, in contrast with the low-energy emission band that displays a very large Stokes shift around 300 nm. This could indicate that the transition corresponding to the low energy band is forbidden, in agreement with the results derived from the Tauc plot (see Fig. 3B). The low-energy emission band shows a blue shift of the excitation band ($\lambda \approx 245$ nm) and a small red shift of the emission band ($\lambda \approx 635$ nm) at lower pH values (pH ≈ 9) as it can be seen in SI Fig. S7a. The high-energy band is very sensitive to the R2 = [SH]/[Au(III)] ratio and completely disappears for R2 ⩽ 2.07,

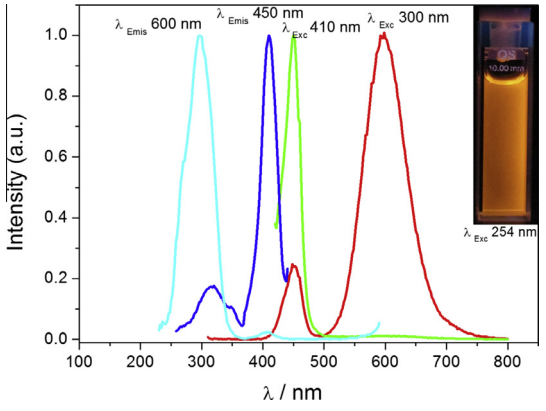

Fig. 6. Luminescent properties of Au clusters synthesized in nanosomes at pH ≈ 12.

as it will be described in detail later on. It was also observed that the intensity of the low-energy emission increases with aging attaining a stable level only after ≈100 days, as it can be seen in SI Fig. S7b showing the evolution of the photoluminescence in aged samples.

The fluorescence decay curves recorded by excitation at 300 nm or 410 nm are complex and can only be fitted with a sum of three exponentials (see SI Figs. S8a and S8b). The lifetimes, τ_i, and the corresponding amplitudes, a_i, (in%) obtained by fitting the decay curve, recorded at 450 nm, are: $\tau_1 = 0.25$ ns (46%), $\tau_2 = 1.4$ ns (39%); $\tau_3 = 6.5$ ns (15%). The observed lifetimes are typical of those found in the literature for the luminescence decay of small clusters [4,18,37]. The decay recorded at the maximum of the low energy emission band at 600 nm is very long, with lifetimes and corresponding amplitudes (in%): $\tau_1 = 8$ ns (11%), $\tau_2 = 440$ ns (34%); $\tau_3 = 5.7$ μs (55%).

The obtained photoluminescent gold clusters show very good colloidal stability, being possible to evaporate the water under vacuum and to redisperse them again maintaining intact their luminescent properties. Traditional organic dyes usually show fast photobleaching compared to quantum dots, which have much better photostability. In general, gold clusters are also very photostable [8]. In SI Fig. S9 it can be seen that the clusters here produced are also very resistant to photobleaching.

The luminescence quantum yield calculated in water at room temperature is 1.2% for the non-long aged samples and approx. 3–4 times larger for the long-aged samples, using as reference a 0.1 M solution of quinine sulfate dihydrate in H_2SO_4 (fluorescence quantum yield, $\Phi = 0.546$), being highly enough to be used as biolabels [8]. It has to be added that the reaction for the production of the photoluminescent gold clusters is very easy to scale up (we obtained clusters with similar luminescent properties using a 50 L reactor), and also that the quantum yields can be further increased by a factor of ≈3 introducing a more packed layer in the cluster surface by capping exchange as we will be published elsewhere.

3. Discussion

Mass spectra analysis clearly shows a bimodal cluster size distribution, which is also corroborated by the two-well defined band-gaps (1.8 and 2.9 eV) derived from the optical absorption spectra. This picture is supported as well by the EXAFS results showing two different capping atoms for gold (sulfur and oxygen) assigned to the two clusters. In addition, the fitted Au–Au distances are in agreement with the predictions for these two cluster sizes and the data can be fitted with a total coordination number Au–Au compatible with their coexistence. The reason for the formation of two populations of cluster sizes inside the nanosomes could be attributed to the presence of two types of binding sites inside the nanosomes, which select the final sizes of the clusters. Presumably the small clusters are attached to the thiol-terminated palmitic acids, which should be formed inside the strong binding site domains (SH groups) of the nanosomes, in agreement with the fact that thiols can be used to synthesize small clusters due to their strong binding affinity for gold [38]. At the same time, the minimum size of the detected clusters ($Au_{5,6}$) agree with recent results showing that below such sizes clusters do not bind with thiols [39]. The big clusters should then be presumably formed inside the soft binding site domains (OH groups) of the nanosomes. Hence, this type of nanosomes constitutes a nice hybrid capping to obtain this unusual two-cluster population system. It has to be noticed that Shang et al. [17], using dihydrolipoic acids to obtain near-infrared fluorescent gold clusters, mentioned already the advantages of using capping agents with two binding sites.

As we referred in the Introduction the currently accepted mechanism for the large Stokes shifts observed for ligand stabilized gold clusters with a core of Au atoms surrounded by a shell of Au–S staple motifs is based on the presence of LMCT transition. This is the case namely of the most studied Au_{25} SR_{18} cluster whose structure is composed of a icosahedral Au_{13} core and a shell of six –RS–Au–RS–Au–RS– extended staple motifs. However, this explanation can be ruled out in our case because: (1) our clusters are exclusively formed by Au (0), as it was observed by XPS and also corroborated by the fact that by adding more reducing agent no changes in the luminescence are observed, which otherwise would be expected because in the synthesis we used an excess of reducing agent; (2) the formation of LMCT state is usually a very fast process associated with the formation of clusters, so that stable luminescent properties are observed just after the cluster synthesis, which was not observed in our case where the time-evolution of the luminescence is very slow; (3) it would be difficult to explain why LMCT bands are observed only for a particular Au/capping ratio – see Fig. 7 below and the corresponding discussion –; (4) the very long lifetime of 5.7 μs observed in our case (see below) is one order of magnitude larger than the ones observed for LMCT state as it is the case of glutathione-protected gold clusters[40], and so cannot be associated to a LMCT transition.

Therefore, two possible explanations for this large Stokes shift can be envisaged (i) very efficient non-radiative energy transfer from the small absorbing clusters to the larger clusters or (ii) fast relaxation process from a high energy state reached by excitation to attain the emissive state whose transition to the ground state is forbidden. The energy transfer mechanism is not plausible because by direct excitation of the small clusters at 410 nm the emission intensity at 600 nm is very low. This rules out the possibility that the energy levels implied in the luminescence can form a type I heterojunction, i.e., that the band-gap of the large clusters are nested inside the band-gap of the small clusters. The second mechanism seems to be more plausible, being then the emission centered at 600 nm attributed to a cluster–cluster charge transfer complex. This hypothesis is sustained by the electronic configurations deduced from the mass spectrometry analysis, showing that clusters can be found in both close-shell and non-close-shell configurations. Moreover, one can see that large non-close shell clusters (Au_{14} and Au_{16}) can be transformed into close-shell species just by gaining 1 or 2 electrons (see SI Table S2). At the same time, the small non-close shell clusters can be transformed into the close-shell corresponding ones by losing 1 or 2 electrons (see SI Table S2). Therefore, it is very plausible to think about the formation of inter-charge transfer between the small and large non-close shell configuration clusters in order to achieve the most stable close-shell electronic configurations. From SI Table S2 it is further deduced that such electron transfers should occur among the pairs (Au_6–Au_{16}) and (Au_5–Au_{14}). It is to note that such cluster pairs would have an estimated size of 0.5 nm (cluster 5/6) + 0.8 nm (cluster 14/16) = 1.3 nm, which nicely agrees with the averaged TEM particle diameter (1.2 ± 0.2 nm).

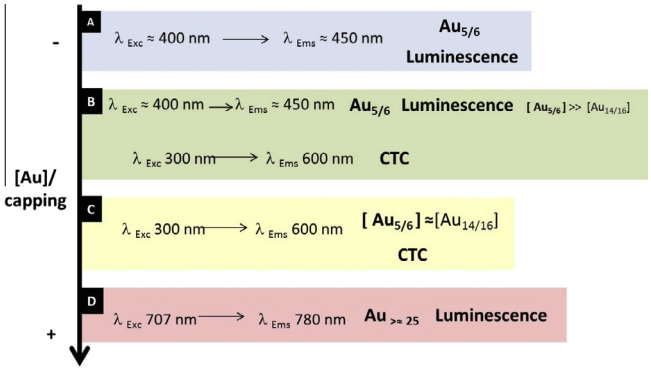

Fig. 7. Schematic representation of the species obtained in the synthesis depending on the concentration of gold salt and their correspondent luminescent properties. A: [Au] = 0.665 mM, R2 = 3.11; B: [Au] = 0.798 mM, R2 = 2.60; C: [Au] = 0.998 mM, R2 = 2.07. D: [Au] = 1.27 mM, R2 = 1.56, being R2 = [SH]/[Au(III)]. CTC: Charge transfer complexes.

The probability that a pair of small and large clusters will be formed at the interfaces between the thiol and hydroxyl domains is very small: 0.71% for these conditions (see calculations given in the SI). This estimation was obtained after considering that all the Au atoms are distributed forming an equal amount of the two major populations of clusters observed in the mass spectra ($Au_{5/6}$ and $Au_{14/16}$). Because we assume that initially separated thiol and hydroxyl domains are formed inside the nanosome, $Au_{5/6}$ clusters will be segregated in the thiol domain while $Au_{14/16}$ clusters will be in the hydroxyl domain. The pair formation will occur when both clusters are present at the interface between the two domains. Therefore, only after very inhibited Brownian motion of the (small and large) formed clusters inside the nanosome film by the encounter of small and the corresponding large clusters (i.e. 6–16, 5–14) can be built up stable cluster pairs, as schematically shown in SI Fig. S10. After that, the electronic stabilized cluster pairs, protected by the bola lipids can migrate out of the nanosomes forming species having a size of approximately 1.2 nm, with a number of atoms close to 25 (19, for the 5–14 pair couple and 22 for the 6–16 pair couple) as it is observed in the TEM pictures for the purified clusters (Fig. 5 and SI S4).

According to this interpretation, the luminescence associated with the formation of such cluster pairs (formed by the appropriate association of small and large clusters) will not appear just at the end of the synthesis, because the probability to form such clusters as close neighbors is very low (less than 1%, as we deduced above), but after some aging time needed for such assumed rearrangements (as it is schematically depicted in SI Fig. S10). And this is what actually happens: such large Stokes shift luminescence only appears after several minutes, but the intensity slowly evolves during about two months (having a relaxation time of ≈25 days, as it is shown in SI Fig. S11) to achieve the final maximum intensity (see SI Figs. S7b and S11). The estimated *effective* diffusion coefficient for such rearrangements is extremely low ($\approx 10^{-11}$ cm^2 s^{-1}, see the estimations in the SI), which indicates not only the very slow Brownian motion of clusters attached to the bola lipids in the nanosome film, but also the small probability for *effective* collisions between the clusters having the appropriate electronic structures (5/14 and 6/16) to give the stable charge transfer complex (see SI Table S4). Lateral diffusion coefficients of lipids in bilayers are usually in the range 10^{-7}–10^{-9} cm^2 s^{-1} (see e.g. [41]). Therefore, assuming similar values for the cluster-attached bola lipids in the nanosomes, the activation energy, $\Delta \approx 25$ kcal/mol, for the formation of the charge transfer complexes can be deduced (see SI). Such activation energy could be related to geometrical rearrangements of clusters after the foreseeable fast electron transfer between these sub-nanometer clusters after collision. The cluster–cluster interactions after the formation of such cluster pairs seem to be strong enough at room temperature (or temperatures below 50 °C), because once such luminescence appears it is very stable, and remains for at least two years at room temperature.

To further confirm this hypothesis, we carried out a new set of experiments changing the proportions of gold/cappings (OH or SH) used in the synthesis, because – according to the previous interpretation- the formation of small clusters should be favored when the ratio SH/gold increases. It is observed that the formation of mainly small size clusters with a high-energy emission band at 450 nm is favored when the concentration of gold salt is lower than the one used in the experiments previously showed, as long

as we maintain the cappings in the same proportion, and only a small amount of cluster–cluster charge transfer complexes with the low-energy emission peak at 600 nm are formed (SI Fig. S12). If the concentration of gold is increased in approx. 20%, the concentration of small clusters decreases, (SI Fig. S13), and the proportion of cluster–cluster charge transfer complexes increase, being now the high-energy and low-energy emissions, at 450 nm and 600 nm, approximately equal. If the concentration of gold is further increased in approx. 50% (SI Fig. S14) one can obtain mainly cluster–cluster charge transfer complexes and only the low-energy emission is observed. Finally, if the concentration of gold salt is raised further up in approx. 100%, only the formation of large clusters is observed. In this case, the size of the large clusters also increases, as it is deduced by a red shift in the luminescence emission (λ_{em} = 780 nm = 1.6 eV; see SI Fig. S15) together with an almost continuum decay in the UV–vis spectrum, which can be associated to the formation of mainly clusters of >≈25 atoms [$N = (5.32/1.6 - 0.4)^3 = 25$] [42]. These results are summarized in Fig. 7, and clearly indicate the critical conditions for achieving such equal proportions of small and large non-closed shell clusters needed for the formation of the assumed cluster–cluster charge transfer complexes.

According to this, a possible explanation of all the photoluminescent results – including the photoluminescent decay curves – can be put forward, as it is schematized in Fig. 8 (for simplicity we consider only the pair Au_5–Au_{14}, but the discussion should be similar for the Au_6–Au_{16} pair), making the following assumptions: (1) for large clusters the Fermi level coincides with the bulk Femi level, then: $E_{Fermi}\,(Au_{14}^{-3}) \approx E_{Fermi}\,(Au_{14}^{-4})$; (2) for small clusters the Fermi level increases with a power law behavior, as it was reported before [26,43] ($E_{Fermi}\,(Au_N) \approx E_{Fermi}\,(bulk) + CN^{-1/3}$, $C \approx 5$ eV) having the cluster's stability (and, therefore, the corresponding Femi levels) an even-odd alternation: $E_{Fermi}\,(Au_5^{-1})_{even\ n.\ of\ e-} \approx E_{Fermi}\,(Au_5^{-2})_{odd\ n.\ of\ e-} + 2$ eV [44].

The observed photoluminescent decays can be now interpreted using this Scheme. The short lifetime of 8 ns is attributed to a singlet–singlet radiative sp–d interband recombination, while the 440 ns lifetime is attributed to a triplet–singlet transition within the sp band of the isolated large clusters of 14/16 Au atoms [45]. The very long lifetime of 5.7 μs is attributed to the emission of the cluster–cluster charge transfer complex (see SI Fig. S8b). Despite the amplitudes of all components being significant, the luminescence spectrum is dominated (>95%) by the 5.7 μs component due to its very long lifetime. The long-lived emission is in agreement with the fact that the corresponding absorption in the UV–vis spectrum is not detectable pointing to a forbidden transition. The emission is still inhibited by the need that one electron has to be transferred from the filled 1D band of the large cluster to the 1P band of the small cluster prior to emission in order to create an empty level in the 1D band (see Fig. 8). The 2S–1D transition is forbidden in the large clusters but not in the small ones, which can be explained by the fact that the large clusters $Au_{14/16}$ has a tetrahedral symmetry with a very large (~2.5 Å) hollow cage, while the $Au_{5,6}$ clusters are planar. We cannot observe the rise time components observed recently by Stamplecoskie et al. [22,40] corresponding to the fast relaxation processes from the high excited state reached upon excitation because the process is too fast to be recorded by our *time-correlated single-photon counting* (TCSPC), whose time resolution is of about 5 ps.

4. Conclusion

We have synthesized water-soluble luminescent gold clusters in nanosomes exhibiting long lifetime luminescence and very large Stokes shift. The resulting Au clusters are very resistant to photobleaching and have a luminescence quantum yield around 1–5%. It was observed that their luminescent properties cannot be explained by the currently assumed mechanism based on the presence of LMCT absorptions. A plausible cluster–cluster charge transfer complex with a stable electronic closed-shell configuration is proposed for explaining their interesting luminescent properties. The two different groups of the fatty acids (OH and SH) are assumed to act as templating cappings for the formation of the complex precursor cluster pairs. The external functional groups of the bola lipids (COO–) make the luminescent cluster complexes not only soluble in water, but also suitable to be used for the conjugation of biomolecules. Therefore, the mechanism here described could be used as a general strategy, opening new ways of fabricating stable *atom-level quantum dots* with large Stokes shifts of great importance in many sensor applications.

5. Experimental section

5.1. Synthesis

All glassware was washed with Aqua Regia and rinsed thoroughly with ethanol and ultrapure water prior to their use.

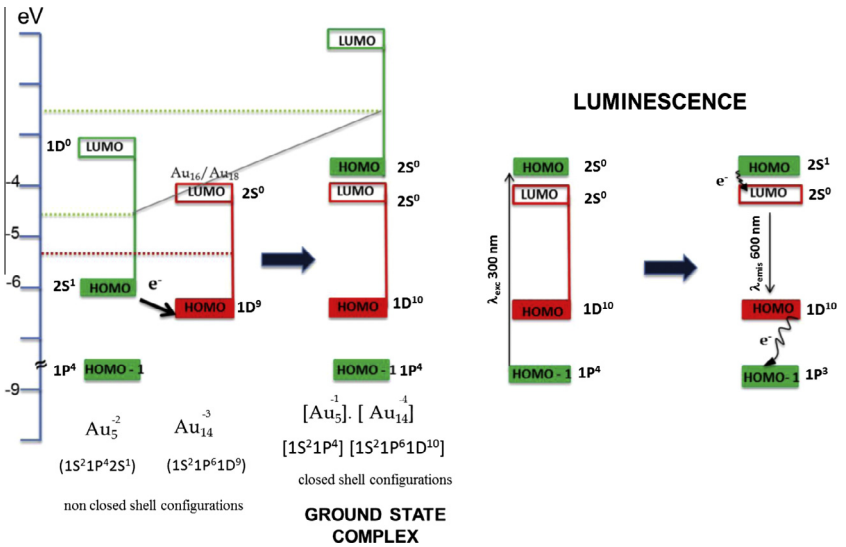

Fig. 8. Schematic representation of the possible distribution of energy levels in the formed $(Au_5)^{-2}$ and $(Au_{14})^{-3}$ clusters, and the charge transfer complexes $(Au^5)^{-1}\cdot(Au_{14})^{-4}$.

Gold clusters were obtained in nanosomes using the following procedure: First, nanosomes were formed by mixing mercapto (90%, Aldrich) and/or hydroxyl (98% Aldrich) palmitic acid-tetrabutyl ammonium salts (TBAOH solution, 40% in water, Fluka) in water. Typically, in a conical flask containing 5.4 mL of milli-Q water, aqueous hydroxyl palmitic acid solution (2 mL, 10 mg/mL) was mixed with aqueous mercapto palmitic acid solution (0.622 mL, 10 mg/mL) and the necessary volume of tetrabutyl ammonium hydroxide until neutralization under vigorous stirring. The resulting nanosomes solution was aged for 2 min and then a volume of 400 μL of $HAuCl_4{\cdot}3H_2O$ (gold (III) chloride hydrate, 99.999% metals basis, Aldrich) solution (5 mg/mL) was added with the subsequent reduction by adding 400 μL of $NaBH_4$ solution (0.05 M). This nanosome/gold stock solution mixture was then stirred and incubated at 35 °C for 1 h, turning from colorless to pale brown and aged during ≈3 h. Then, the resulting cluster solution was passed through a Whatman 0.45 μm syringe tip filter in order to eliminate the excess of fatty acids leading to a stable transparent solution. This cluster solution was aged during approx. 3 months for achieving the final stable photoluminescent properties. For characterization studies clusters were extracted from the nanosome solutions by ultracentrifugation (80000 rpm, 50 min, Beckman Coulter).

5.2. Optical characterization

UV–vis absorption spectra were obtained at room temperature using a Hewlett-Packard HP8452A spectrophotometer in a 1 mm × 1 cm × 3 cm quartz cuvette.

The steady state fluorescence measurements and the photobleaching experiment were also carried out at room temperature using a Varian Cary Eclipse spectrofluorimeter in a 1 cm × 1 cm × 3 cm quartz cuvette. Both excitation and emission spectra were collected using a Xenon flash lamp (excitation and emission bandwidths of 5 nm) using adequate filters to eliminate artifacts, namely the presence of the second order excitation line in the luminescence spectra.

Time-resolved picosecond fluorescence measurements were performed by the time-correlated single-photon counting (TCSPC) technique using ps-laser excitation. Two laser setups were used: one for excitation at 300 nm consisted of a mode-locked Spectra-Physics Nd:YVO4 diode laser (Vanguard 2000-HM532), delivering 2 W of 532 nm light at a repetition rate of 76 MHz and pulse duration of ≈12 ps that synchronously pumped a cavity dumped rhodamine 6G dye laser (Coherent 701-2 dye laser, delivering ~40 nJ pulses of 5–6 ps). The laser repetition rate was set to 3.45 MHz for the short decays (ns time range) or to 210 kHz for the long decays (μs time range). For excitation at 390 nm a new setup consisting of a $Nd:YVO_4$ diode laser (Spectra-Physics Millenia XS 10 W at 532 nm) pumping a Spectra-Physics Tsunami titanium-sapphire laser, delivering 100 fs pulses at a repetition rate of 76 MHz was used. The laser light from both set-ups was frequency doubled using a LBO crystal to obtain laser light of 300 nm or 390 nm for excitation. The intensity decay measurements were made by an alternate collection of impulse and decay, with the emission polarizer set at the magic angle position. Impulse was recorded slightly away from the excitation wavelength with a scattering suspension. For the decays a cutoff filter was used, effectively removing all excitation light. The emission wavelength was selected by a Jobin-Yvon HR320 monochromator with a grating of 100 lines/nm, and was detected by a Hamamatsu 2809U-01 micro-channel plate photomultiplier as a detector. The instrument response function had an effective fwhm of 35 ps. The decay curve analysis was made by an iterative deconvolution method that considers the possibility of incomplete decays.

5.3. Mass spectrometry

ESI-TOF experiments have been done on a Bruker Microtoff instrument. Two different sources were tested: a conventional ESI sprayer, and a micro-flow with narrower capillary sprayer (internal diameter less than half of that used in conventional ESI sprayer). Both, conventional sprayer and micro-flow sprayer sources were assisted by N_2 at 2 and 2.5 bar, respectively. The high voltage applied to the upstream stainless-steel capillary was 4.5 kV. The mass spectrometer was programmed to record the ion signals in negative mode. Samples were introduced by direct injection after dilution in methanol 1:1. Results in the low mass range were obtained by using micro-flow at 5 μL/min. More details about the used technique and the peak identification are given in the SI.

5.4. EXAFS

Au L_3-edges EXAFS (Extended X-ray Absorption Fine Structure) spectra were measured at room temperature in fluorescence mode at the XAFS2 beamline at the Laboratorio Nacional de Luz Síncrotron (LNLS, Campinas, Brazil). The solution of gold clusters in water was disposed in a quartz capillary at 45° of the incident beam direction. The EXAFS oscillations $\chi(k)$ were extracted from the experimental data with standard procedures using the Athena program, part of the IFEFFIT package [Ravel, B.; Newville, M. *J. Synchrotron Rad.* 2005, *12*, 537]. The Fourier transformation was calculated using the Hanning filtering function. The k^2 weighted $\chi(k)$ data, to enhance the oscillations at higher k, were Fourier transformed. EXAFS modeling was carried out using the ARTEMIS program, which is also part of the IFFEFIT package. Structural parameters (coordination numbers and bond lengths and their mean squared disorders) were obtained by a nonlinear least-squares fit of the theoretical EXAFS signal to the data in R space by Fourier transforming both the theory and the data. Theoretical scattering path amplitudes and phase shifts for all paths used in the fits were calculated using the FEFF6 code [Zabinski, S.I.; Rehr, J.J.; Ankudinov, A.; Albers, R.C.; Eller, M. J., Phys. Rev. B 1995, 52, 2995]. The k-range was set from 2.5 to 12 $Å^{-1}$ and the Fourier transform were fitted in the region between 1.2 and 3.4 Å. The passive reduction factor S_0^2 was restrained to values of 0.95. This value was obtained from fitting of metallic Au foil standard by constraining the coordination number in this compound to known crystal structure ones.

5.5. TEM

Nanosomes were imaged with a PHILIPS CM-12 transmission electron microscope at 100 kV using the negative staining method. A drop of the nanosome solution was spread on a 400-mesh copper grid coated with a Formvar film, and the extra droplet was instantly wiped off by filter paper. After being naturally desiccated, a drop of 2% phosphotungstic acid solution was dropped on the copper grid for about 60 s and the extra droplet was also removed. Then the grid was left for drying for about 3 h before TEM observation.

HRTEM micrographs were taken with a Microscope FEI Tecnai Osiris. For HRTEM images an Orius CCD (4x2K) camera was used.

5.6. HR-STEM

HR-STEM was carried out with a TITAN low base 60–300 kV microscope provided with a spherical aberration CEOS corrector for the electron probe allowing us to obtain a probe size below 1 Å. High Angle Annular Dark Field (HAADF) STEM images were recorded from 4 s up to 16 s each.

5.7. XPS

Analysis of the samples was performed using an Thermo Scientific K-Alpha ESCA instrument equipped with aluminum Ka1,2 monochromatized radiation at 1486.6 eV X-ray source. Due to the non-conductor nature of samples it was necessary to use an electron flood gun to minimize surface charging. Neutralization of the surface charge was performed by using both a low energy flood gun (electrons in the range 0–14 eV) and a low energy Argon ions gun. The XPS measurements were carried out using monochromatic Al-K radiation (1486.6 eV). Photoelectrons were collected from a take off angle of 90° relative to the sample surface. The measurement was done in a Constant Analyser Energy mode (CAE) with 100 eV pass energy for survey spectra and 20 eV pass energy for high-resolution spectra.

Acknowledgments

This work was supported by the MCI, Spain (MAT2010-20442; MAT2011-28673-C02-01), MINECO, Spain (MAT2012-36754-C02-01), Xunta de Galicia (Grupos Ref. Comp. GRC2013-044, FEDER Funds), Obra Social Fundación La Caixa (OSLC-2012-007), LNLS (Brazil, Proyect XAFS1 – 17190) and CONICET (PIP N° 112-201101-01035).

Appendix A. Supplementary material

Supplementary data associated with this article can be found, in the online version, at http://dx.doi.org/10.1016/j.jcis.2015.05.042.

References

[1] C.-C. Huang, Z. Yang, K.-H. Lee, H.-T. Chang, Angew. Chem. Int. Ed. 46 (2007) 6824–6828.
[2] H. Tsunoyama, N. Ichikuni, H. Sakurai, T. Tsukuda, J. Am. Chem. Soc. 131 (2009) 7086–7093.
[3] P. Crespo, R. Litran, T.C. Rojas, M. Multigner, J.M. de la Fuente, J.C. Sánchez-López, M.A. García, A. Hernando, S. Penadés, A. Fernández, Phys. Rev. Lett. 93 (2004). 087204-1-4.
[4] B. Santiago González, M.J. Rodríguez, M.C. Blanco, J. Rivas, M.A. López-Quintela, J.M. Gaspar Martinho, Nano Lett. 10 (2010) 4217–4221.
[5] T.G. Schaaff, R.L. Whetten, J. Phys. Chem. B 104 (2000) 2630–2641.
[6] M. Vollmer, U. Kreibig, Optical Properties of Metal Clusters, Springer Series in Material Sciences; Springer, Berlin, 1994.
[7] K.-M. Meiwes-Broer, Metal clusters at surfaces, Structure, Quantum Properties, Physical Chemistry; Springer Series in Cluster Physics, Springer, Berlin, 2000.
[8] C.-A.J. Lin, T.-Y. Yang, C.-H. Lee, S.H. Huang, R.A. Sperling, M. Zanella, J.K. Li, J.-L. Shen, H.-H. Wang, H.I. Yeh, W.J. Parak, W.H. Chang, ACS Nano 3 (2009) 395–401.
[9] L. Polavarapu, M. Manna, Q.-H. Xu, Nanoscale 3 (2011) 429–434.
[10] J. Zheng, C. Zhang, R.M. Dickson, Phys. Rev. Lett. 93 (2004). 077402-1-4.
[11] C.-C. Huang, C.-K. Chiang, Z.-H. Lin, K.-H. Lee, H.-T. Chang, Anal. Chem. 80 (2008) 1497–1504.
[12] Y. Shichibu, K. Konishi, Small 6 (2010) 1216–1220.
[13] E.-S. Shibu, T. Pradeep, Chem. Mater. 23 (2011) 989–999.
[14] P. Biang, J. Zhou, Y. Liu, Z. Ma, Nanoscale 5 (2013) 6161–6166.
[15] Y. Kong, J. Chen, F. Gao, R. Brydson, B. Johnson, G. Heath, Y. Zhang, L. Wu, D. Zhou, Nanoscale 5 (2013) 1009–1017.
[16] C.-C. Huang, C.-T. Chen, Y.-C. Shiang, Z.H. Lin, H.-T. Chang, Anal. Chem. 81 (2009) 875–882.
[17] Li. Shang, N. Azadfar, F. Stockmar, W. Send, V. Trouillet, M. Bruns, D. Gerthsen, G.U. Nienhaus, Small 7 (2011) 2614–2620.
[18] Z. Wu, R. Jin, Nano Lett. 10 (2010) 2568–2573.
[19] J. Zheng, C. Zhou, M. Yu, J. Liu, Nanoscale 4 (2012) 4073–4083.
[20] Y. Chen, T. Yang, H. Pan, Y. Yuan, L. Chen, M. Liu, K. Zhang, S. Zhang, P. Wu, J. Xu, J. Am. Chem. Soc. 136 (2014) 1686–1689.
[21] J. Sun, H. Wu, Y. Jin, Nanoscale 6 (2014) 5449–5457.
[22] K.G. Stamplecoskie, Y.-S. Chen, P.V. Kamat, J. Phys. Chem. C 118 (2014) 1370–1376.
[23] M.A.H. Muhammed, A.K. Shaw, S.K. Pal, T. Pradeep, J. Phys. Chem. C 112 (2008) 14324–14330.
[24] P.L. Xavier, K. Chaudhari, P.K. Verma, S.K. Pal, T. Pradeep, Nanoscale 2 (2010) 2769–2776.
[25] J. Tauc, R. Grigorovici, A. Vancu, Phys. Stat. Sol. 15 (1966) 627–637.
[26] N. Vilar-Vidal, J. Rivas, M.A. López-Quintela, ACS Catal. 2 (2012) 1693–1697.
[27] B. Santiago-González, M.A. López-Quintela, New Strategies and Synthetic Routes to Synthesize Fluorescent Atomic Quantum Clusters. In Functional Nanometer-Sized Clusters of Transition Metals: Synthesis, Properties and Applications. Wei Chen, Shaowei Chen (Ed.), RSC Smart Materials No. 7. RSC, 2014, pp. 25–50 (Chapt. III).
[28] H. Qian, Y. Zhu, Proc. Natl. Acad. Sci. U.S.A. 109 (2012) 696–700.
[29] M. Walter, J. Akola, O. López-Acevedo, P.D. Jadzinsky, G. Calero, C. Ackerson, R.L. Whetten, H. Grönbeck, H. Häkkinen, Proc. Natl. Acad. Sci. U.S.A. 105 (2008) 9157–9162.
[30] H. Häkkinen, Chem. Soc. Rev. 37 (2008) 1847–1859.
[31] O. Varnavski, G. Ramakrishna, J. Kim, D. Lee, T. Goodson, J. Am. Chem. Soc. 132 (2010) 16–17.
[32] Z. Wu, J. Suhan, R. Jin, J. Mater. Chem. 19 (2009) 622–626.
[33] N. Vilar-Vidal, M.C. Blanco, M.A. López-Quintela, J. Rivas, C. Serra, J. Phys. Chem. C 114 (2010) 15924–15930.
[34] I. Joseph, I. Besnard, M. Rosenberger, B. Guse, H.-G. Nothofer, J.M. Wessels, U. Wild, A. Knop-Gericke, D. Su, R. Schlögl, A. Yasuda, T. Vossmeyer, J. Phys. Chem. B 107 (2003) 7406–7413.
[35] M.P. Casaletto, A. Longo, A. Martorana, A. Prestianni, A.M. Venezia, Surf. Interface Anal. 38 (2006) 215–218.
[36] B. Vincent Christ, Handbook of Elements and Native Oxides, XPS International, Inc., 1999.
[37] M.A.H. Muhammed, S. Ramesh, S.S. Sinha, S.K. Pal, T. Pradeep, Nano Res. 1 (2008) 333–340.
[38] R. Jin, Nanoscale 2 (2010) 343–362.
[39] A. Corma, P. Concepción, M. Boronat, M.J. Sabater, J. Navas, M.J. Yacaman, E. Larios, A. Posadas, M.A. López-Quintela, D. Buceta, E. Mendoza, G. Guilera, A. Mayoral, Nat. Chem. 5 (2013) 775–781.
[40] K.G. Stamplecoskie, P.V. Kamat, J. Am. Chem. Soc. 136 (2014) 11093–11099.
[41] G. Lenaz, Biosci. Rep. 7 (1987) 823–837.
[42] M.A.H. Muhammed, P.K. Verma, S.K. Pal, R.C.A. Kumar, S. Paul, R.V. Omkumar, T. Pradeep, Chem. Eur. J. 15 (2009) 10110–10120.
[43] B. Assadollahzadeh, P. Schwerdtfeger, J. Chem. Phys. 131 (2009). 064306-1-11.
[44] E.M. Fernández, J.M. Soler, I.L. Garzón, L.C. Balbás, Phys. Rev. B 70 (2004). 165403-1-14.
[45] J. Zheng, J.T. Petty, R. Dickson, J. Am. Chem. Soc. 125 (2003) 7780–7781.